Microorganism microneedle micro-engine depth drug delivery

Bin Zheng [1,2,10] ✉, Qiuya Li[1,10], Laiping Fang[3,10], Xiaolu Cai[4,10], Yan Liu[5], Yanhong Duo[5], Bowen Li [1], Zhengyu Wu[1], Boxi Shen[6], Yang Bai[1,7] ✉, Shi-Xiang Cheng[8] ✉ & Xingcai Zhang [9] ✉

As a transdermal drug delivery method, microneedles offer minimal invasiveness, painlessness, and precise in-situ treatment. However, current microneedles rely on passive diffusion, leading to uncontrollable drug penetration. To overcome this, we developed a pneumatic microneedle patch that uses live *Enterobacter aerogenes* as microengines to actively control drug delivery. These microbes generate gas, driving drugs into deeper tissues, with adjustable glucose concentration allowing precise control over the process. Our results showed that this microorganism-powered system increases drug delivery depth by over 200%, reaching up to 1000 μm below the skin. In a psoriasis animal model, the technology effectively delivered calcitriol into subcutaneous tissues, offering rapid symptom relief. This innovation addresses the limitations of conventional microneedles, enhancing drug efficiency, transdermal permeability, and introducing a creative paradigm for on-demand controlled drug delivery.

Microneedle transdermal drug delivery is a non-invasive technique for delivering minute amounts of drugs through the skin. By penetrating the stratum corneum, this technology facilitates the easier penetration of drugs into the skin and their entry into the circulatory system. The application of this technology enhances drug absorption and bioavailability, effectively reducing the required dosage and drug concentration[1]. In addition, the design of microneedles imparts sustained-release characteristics, transforming them into miniature drug depots capable of slowly releasing drugs over a specified period[2]. This slow-release feature not only provides a more stable and prolonged therapeutic effect but has also led to significant breakthroughs in various fields such as drug delivery, vaccine administration[3], and gene transfer[4]. Despite the unique advantages of microneedle transdermal drug delivery in the field of drug administration, the most widely adopted type of microneedles currently is still the dissolvable type[5]. These microneedles facilitate the free diffusion of drugs loaded within them into the skin through the dissolution process of the microneedle matrix. While it is possible to control the rate of drug release by adjusting the matrix composition—an area of primary focus for many researchers—once the microneedle dissolves and the drug enters the body, the drug relies solely on its own passive diffusion[6]. At this point, the microneedle can no longer serve any regulatory function. Therefore, in situations where targeting specific sites or deep-seated lesions is necessary, traditional dissolvable microneedles still lack precise control over penetration depth and diffusion range after releasing drugs into the body[7]. The key feature of microneedles is their painless and minimally invasive nature, making it impractical to blindly increase the length of the needle solely to enhance drug penetration

[1]Academy of Medical Engineering and Translational Medicine, Tianjin University, Tianjin, China. [2]School of Biomedical Engineering and Technology, Tianjin Medical University, Tianjin, China. [3]Guangdong Second Provincial General Hospital, School of Medicine, Jinan University, Guangzhou, China. [4]Department of Biomedical Engineering, College of Life Science and Technology, Huazhong University of Science and Technology, Wuhan, China. [5]School of Engineering and Applied Sciences, Harvard University, Cambridge, Massachusetts, USA. [6]School of Pharmaceutical Science and Technology, Tianjin University, Tianjin, China. [7]Department of Stomatology, Tianjin Medical University General Hospital, Tianjin, China. [8]Healthina Academy of Cellular Intelligence Manufacturing & Neurotrauma Repair of Tianjin Economic-Technological Development Area, TANGYI Biomedicine (Tianjin) Co. Ltd (TBMed), Tianjin, China. [9]Department of Materials Science and Engineering, Stanford University, Stanford, CA, USA. [10]These authors contributed equally: Bin Zheng, Qiuya Li, Laiping Fang, Xiaolu Cai. ✉e-mail: binzheng@tju.edu.cn; bystomatology@163.com; shixiangcheng@vip.126.com; xingcai@stanford.edu

depth. These limitations restrict the current application of traditional dissolvable microneedles in cases involving thickened skin or deep tissue penetration[8]. Hence, there is an urgent need to design and develop a strategy that can enhance the active depth penetration and diffusion of drugs at the microneedle level.

Currently, many researchers in the field of microneedles are dedicated to achieving more precise control over the release of drugs, such as controlling the rate, timing, and dosage of drug release[9,10]. This has led to the emergence of various additional therapies, including external control methods like magnetic fields and light-based controls[9]. However, these external control[10] methods require device regulation, which can be inconvenient, operationally cumbersome, and costly, making them unsuitable for diverse environments, including home use. Some researchers are also focusing on modifying the drugs carried by microneedles themselves. For example, incorporating targeting modules[11] combined with drugs is one approach, with the hope of thereby regulating the direction of drug diffusion within the body after release. However, the introduction of additional targeting modules or specific modifications for drugs undoubtedly introduces more components with safety concerns, hindering a more widespread application[12]. Gas therapy has gradually entered the researchers' field of vision in recent years. Using harmless gas components not only results in fewer residues but also allows some beneficial gas components to play a role in adjunctive therapy[13]. The gas itself has enormous potential as a driving force. If gas power at the physical level can be utilized to control drug release, imparting the ability for active transport and diffusion of drugs, it can maximize the purity of the drugs, making their application more versatile. Some scholars have considered utilizing materials to generate gas[14], such as using magnesium-based metallic materials to produce H_2[15] or utilizing oxides to generate O_2[16]. However, the reaction conditions for gas generation from materials are quite stringent, requiring catalysts and incurring high costs. In addition, the total amount of gas produced is limited by the quantity of materials, and the rate of gas generation is confined to a small space that can be controlled artificially. Once the materials are depleted, the reaction cannot sustain itself, severely limiting the sustainability of gas production[17]. We prepared microneedles loaded with two gas-generating materials, MgH_2 and CaO_2, which produced gas in small amounts and for a short duration, as predicted. Concerns about the safety of handling residual products after the reaction also pose challenges to the medical application of gas-producing materials.

Herein, we developed a living microbially triggered gas-powered microneedle micro-engine for controlled drug delivery. By encapsulating active gas-producing microorganisms, specifically *Enterobacter aerogenes ATCC 13048 (E.A.)*, within the microneedles and maintaining their viability and gas-producing capabilities, we sustainably utilize the gas they produce as a propelling force. This propels the drug loaded on the needle tip to penetrate and diffuse into deeper layers of tissues, overcoming the resistance of the dermal layer and reaching deeper sites. Our innovation lies in combining the unique gas-producing mechanism of natural microorganisms with transdermal drug delivery through microneedles, creating a biologically active gas-powered microneedle micro-engine. This microorganism-powered microneedle micro-engine enables drugs to actively diffuse to deep target sites. By regulating the physiological processes of the microorganisms—primarily by adjusting the gas production—we can control the magnitude and rate of the propelling force, thereby achieving controlled drug delivery depth. This living gas-powered microneedle technology is expected to enhance both the depth and efficiency of drug delivery, offering a creative paradigm and solution for on-demand and controllable delivery in microneedle administration (Fig. 1).

The excessive proliferation of keratinocytes is the main cause of epidermal thickening, a hallmark of psoriasis[18]. Therefore, enhancing drug delivery to the epidermis can significantly improve treatment efficiency. Keratinocytes are the primary cell type in the epidermis, and their abnormal proliferation in psoriasis leads to epidermal thickening and the formation of scales. The proliferation rate of epidermal cells in psoriasis patients is significantly faster than that of normal skin cells, causing a rapid accumulation of keratinocytes that cannot shed properly, resulting in the typical psoriasis plaques[19]. This pathological feature necessitates effective drug penetration through the thickened epidermis to achieve therapeutic effects. In our research, we developed a microbe-powered microneedle technology to address this delivery challenge. By encapsulating gas-producing microbes within the microneedles, these microbes continuously generate gas within the skin, providing a unique propulsive force that enables the drug to penetrate deeper into the thickened epidermis and directly target the overproliferating keratinocytes. This not only inhibits abnormal cell proliferation but also reduces inflammation and alleviates psoriasis symptoms.

Results

Microorganisms have the potential to serve as a source of aerodynamic force

Enterobacter Aerogenes (E.A.) can ferment various sugars such as glucose, lactose, and sucrose, producing gas. It primarily inhabits the human and animal intestines, serving as a normal flora in the human body. *E.A.* exhibits a broad temperature adaptability range, thriving between 15–40 °C. In terms of safety and applicable conditions, *E.A.* holds potential for applications in the treatment of human diseases. Genetic evidence suggests that *E.A.* contains hydrogenase proteins (Hyds) that reversibly catalyze H_2 release or absorption, including ferredoxin pyruvate redox reductase (PFOR) and NADH ferredoxin redox reductase (NFOR). The main hydrogen production route is to catalyze H_2 production using NADH as an electron donor during glycolysis using NADH ferredoxin oxidoreductase (NFOR) (Fig. 2a)[20]. However, there is limited research attempting to harness the gas-producing capabilities of *E.A.*. To ascertain whether *E.A.* has the potential to serve as a gas source for microorganism micro-engines, comprehensive research on its gas production components and capabilities is needed. Initially, gas samples produced by *E.A.* were collected and subjected to gas chromatography analysis. Chromatographic results (Fig. 2a, b, and Supplementary Fig. S1) revealed the useful components to be H_2 (6.15%). To further understand *E.A.*'s gas production mechanism, gas production variations were evaluated under different inoculum sizes, substrate concentrations, and cultivation times (Fig. 2c–e). The H_2 content in the gas was detected, and the methylene blue was decolorized through an oxidation-reduction reaction, indirectly reflecting the differences in gas production. The outcomes of our investigation reveal a direct correlation between substrate concentration and cultivation duration with the observed increase in gas production volume, while the influence of inoculum levels on gas production appeared comparatively nominal. Therefore, when using *E.A.* as a gas-producing microorganism micro-engine, we primarily control the gas production quantity and rate through the substrate concentration, specifically the concentration of glucose.

H_2 is a unique component in the gas produced by *E.A.*, not only distinguishable from other air components but also present in a proportion (around 6%) sufficient to serve as an indicator for detection. Consequently, in subsequent experiments, H_2 will be used as an indicator to infer the overall gas production situation. To quantitatively analyze the factors influencing gas production and identify the relatively optimal conditions for gas generation by *E.A.*, we continuously measured gas production and relative maximum gas production rates over time using a hydrogen gas electrode under different substrate concentrations (Fig. 2h–l and Supplementary Fig. S2). The results demonstrate that the highest gas production volume and gas production rate were observed when the substrate glucose concentration
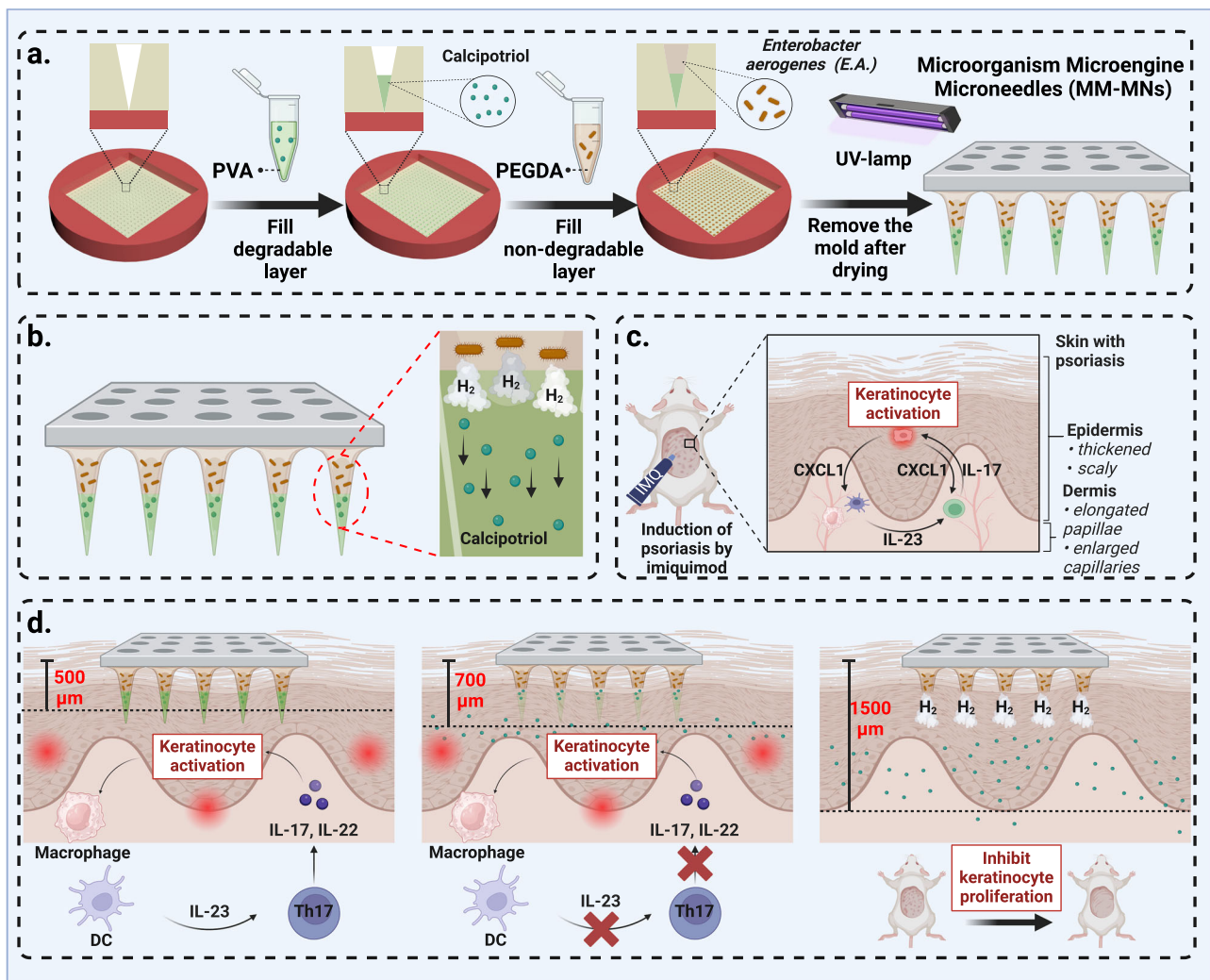
Fig. 1 | Preparation, application principles, and processes of microorganism micro-engine microneedles (MM-MNs). a The preparation process of double-layer microbiota-assisted gas dynamic microneedles. **b** *Enterobacter aerogenes* (*E.A.*) propels the release of drugs from the detachable layer. **c** The pathogenic mechanism of psoriasis. **d** The mechanism of microbiota-assisted gas dynamic microneedles propelling calcipotriol for deep tissue release in the treatment of psoriasis. Created with BioRender.com/w74e852.

was at 20 mg/mL. However, as the substrate concentration continued to increase, there was no statistically significant enhancement in gas production volume and rate; instead, a decline was noted. This phenomenon is postulated to arise from the inhibitory effect of a high glucose environment on the proliferation of *E.A.*, consequently influencing both gas production volume and rate. In a culture medium containing 30 mL of glucose substrate at a concentration of 20 mg/mL, *E.A.* could generate up to 28.7 mL of gas within a 12 h timeframe, with a maximum gas production rate reaching 1.65 mL/s. Moreover, the attainment of the peak gas production rate and volume occurred approximately within the initial 5 to 6 hours following inoculation. Thus, it can be deduced that the optimal conditions for *E.A.* gas production are a substrate concentration of 20 mg/mL, with the maximum gas production rate achieved around 5 to 6 h post-inoculation.

The gas production rate and volume of *E.A.* were found to be considerable. To demonstrate their potential as a microorganism micro-engine, we inoculated the bacteria at the bottom of agar-filled test tubes and sealed them for cultivation. We observed variations in agar displacement distances caused by gas propulsion of different masses (Fig. 2f, g, and Supplementary Fig. S4). The findings reveal that under conditions of substrate concentration at 20 mg/mL and a temperature of 37 °C, after a 12 h cultivation period, *E.A.* is capable of propelling agar with a maximum mass of 4 g, resulting in a

maximum displacement distance of 12 mm. By means of a comprehensive analysis of force and motion, the calculated maximum propulsive force is approximately 0.04 N (where $g = 9.8$ m/s²). In conclusion, these data demonstrate that *E.A.*, as a microorganism capable of producing gas through substrate decomposition, can potentially serve as a microorganism micro-engine for dynamic gas therapy.

Preparation and bacterial activity validation of microorganism micro-engine microneedles (MM-MNs)
The method of transdermal therapy using microneedles loaded with small-molecule drugs or biologics has become quite common. However, encapsulating active microorganisms into microneedles and attempting to harness the continuous production of gas from these active microorganisms[21] to sustain their basic physiological processes poses significant technical challenges. To overcome this hurdle, we conducted a series of characterizations on the matrix composition selection for microneedles, the preparation process, and the validation of microbial activity. The ability of *E.A.* to serve as a source of gas propulsion has been verified. We mixed the bacterial suspension with the substrate glucose and the matrix material poly (ethylene glycol) diacrylate (PEGDA), which is used for fabricating the microneedles, and placed it into a mold. It was solidified using vacuum suction and
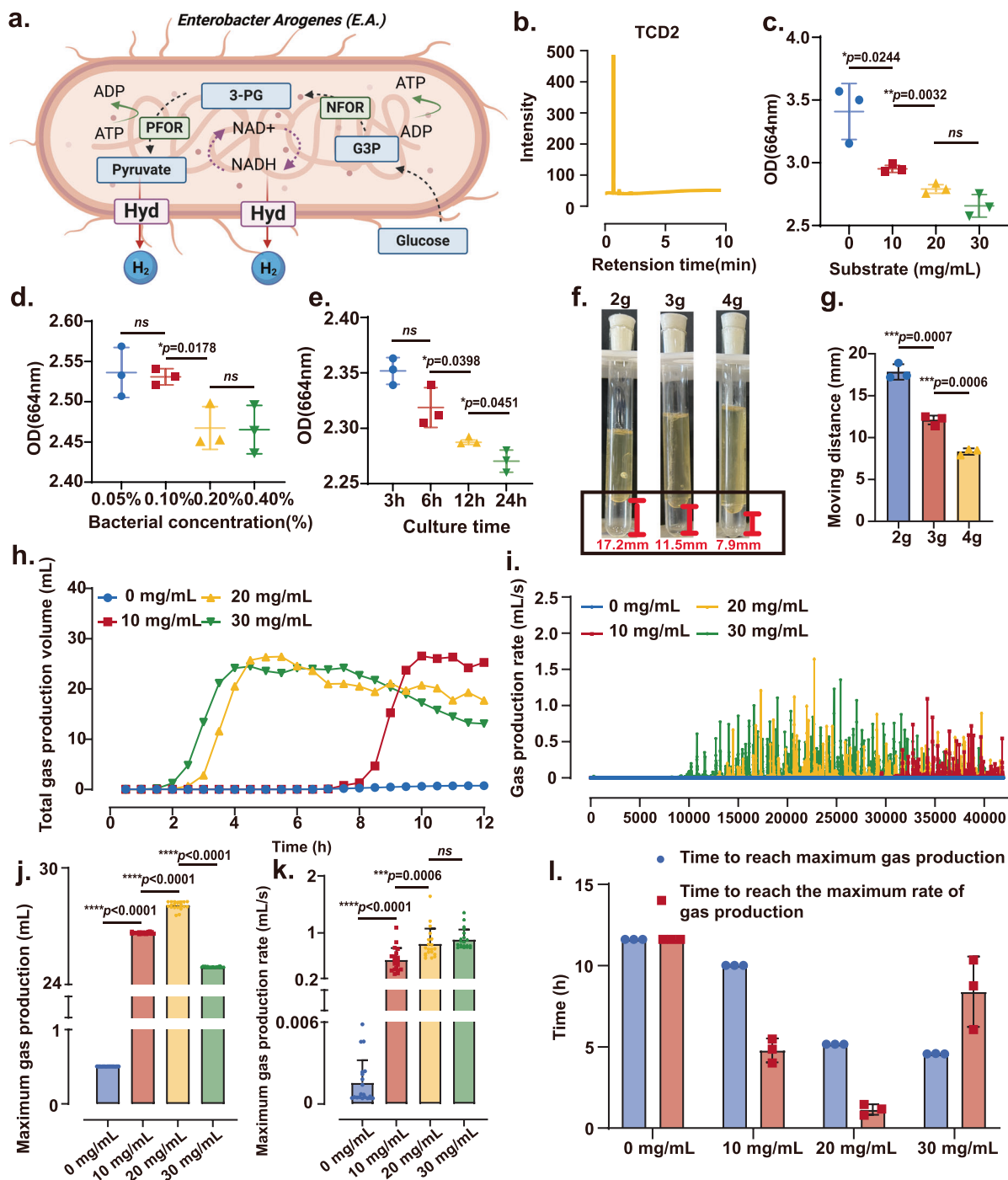
Fig. 2 | Microorganisms have the potential to serve as a source of aerodynamic force. a *E.A.* decomposes substrate glucose to produce H_2. Created with BioRender.com/l25i234. **b** The results of gas chromatographic detection of the mixed gas produced by the *E.A.*. **c**–**e** Changes in H_2 production by the microorganism under different inoculation levels (**c**), substrate concentrations (**d**), and cultivation times (**e**). Mean ± SD of $n = 3$ independent samples. Two-sided Student's t test. **f** The experimental diagram of different masses of agar blocks being pushed by the gas produced by *E.A.*. **g** Effect of *E.A.* produced gas on agar displacement distance of different masses. Mean ± SD of $n = 3$ independent samples. Two-sided Student's t test. **h** Changes in gas production over time under different substrate concentrations. **i** Changes in gas production rate over time under different substrate concentrations. **j** Changes in maximum gas production under different substrate concentrations. **k** Changes in maximum gas production rate under different substrate concentrations. Mean ± SD of $n = 20$ independent samples. Two-sided Student's t test. **l** The time to reach the maximum gas production and gas production rate. Mean ± SD of n = 3 independent samples.

ultraviolet (UV) irradiation (Fig. 3a), thus encapsulating the microorganisms within the microneedles.

To demonstrate the ability of *E.A.* to maintain viability and provide gas propulsion while mixing with the matrix material PEGDA, vacuum suction, and UV curing, we verified the viability of the microorganisms encapsulated in the microneedles. Firstly, we

measured the effect of UV irradiation time on bacterial viability (Fig. 3b). The results showed that although bacterial viability gradually decreased with increasing UV irradiation time, the synthesis process of microorganism micro-engine microneedles (MM-MNs) only required ~5 s of UV irradiation, which had a negligible effect on bacterial viability.
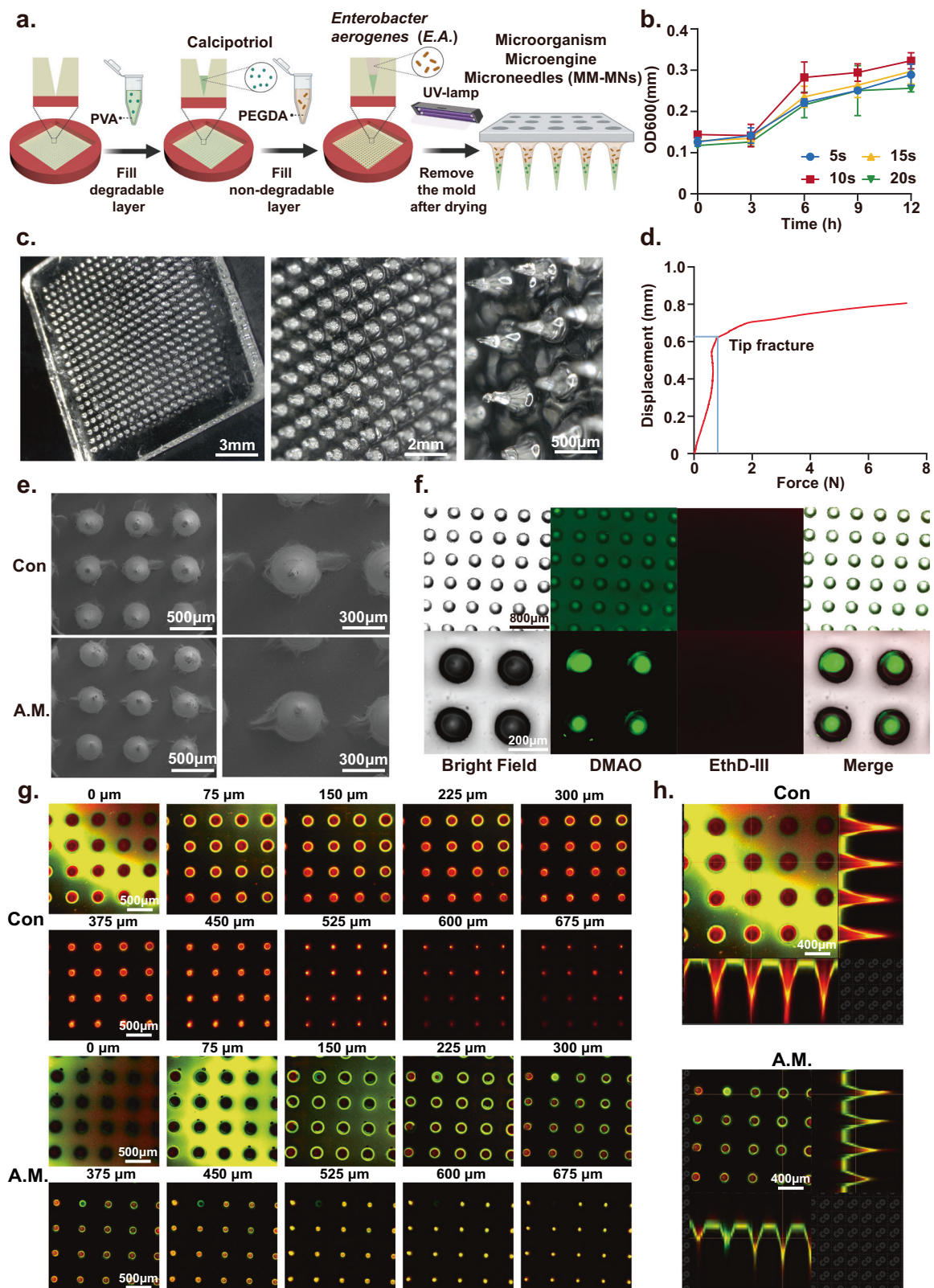
Fig. 3 | Preparation and bacterial activity validation of microorganism microengine microneedles (MM-MNs). a The preparation process of MM-MNs. Created with BioRender.com/e35z291. **b** The effect of ultraviolet irradiation time on the activity of *E.A.*. Mean ± SD of $n = 3$ independent samples. **c** Digital microscopy characterization of microneedle morphology. Scale bar, 3 mm (Left); 2 mm (Middle); 500 μm (Right). **d** Mechanical force for the fracture of the microneedle tips. **e** Scanning electron microscopy characterization of microneedle morphology. Scale bar, 500 μm (Left); 300 μm (Right). **f** Fluorescence microscopy results of *E.A.* activity encapsulated in microneedles. Scale bar, 800 μm (Up); 200 μm (Down). **g**, **h** Confocal microscopy results of *E.A.* activity encapsulated in microneedles. Scale bar, 500 μm (**g**); Scale bar, 400 μm (**h**). A representative image of four biologically independent samples from each group is shown in **c**, **e**, **f**, **g**, and **h**.
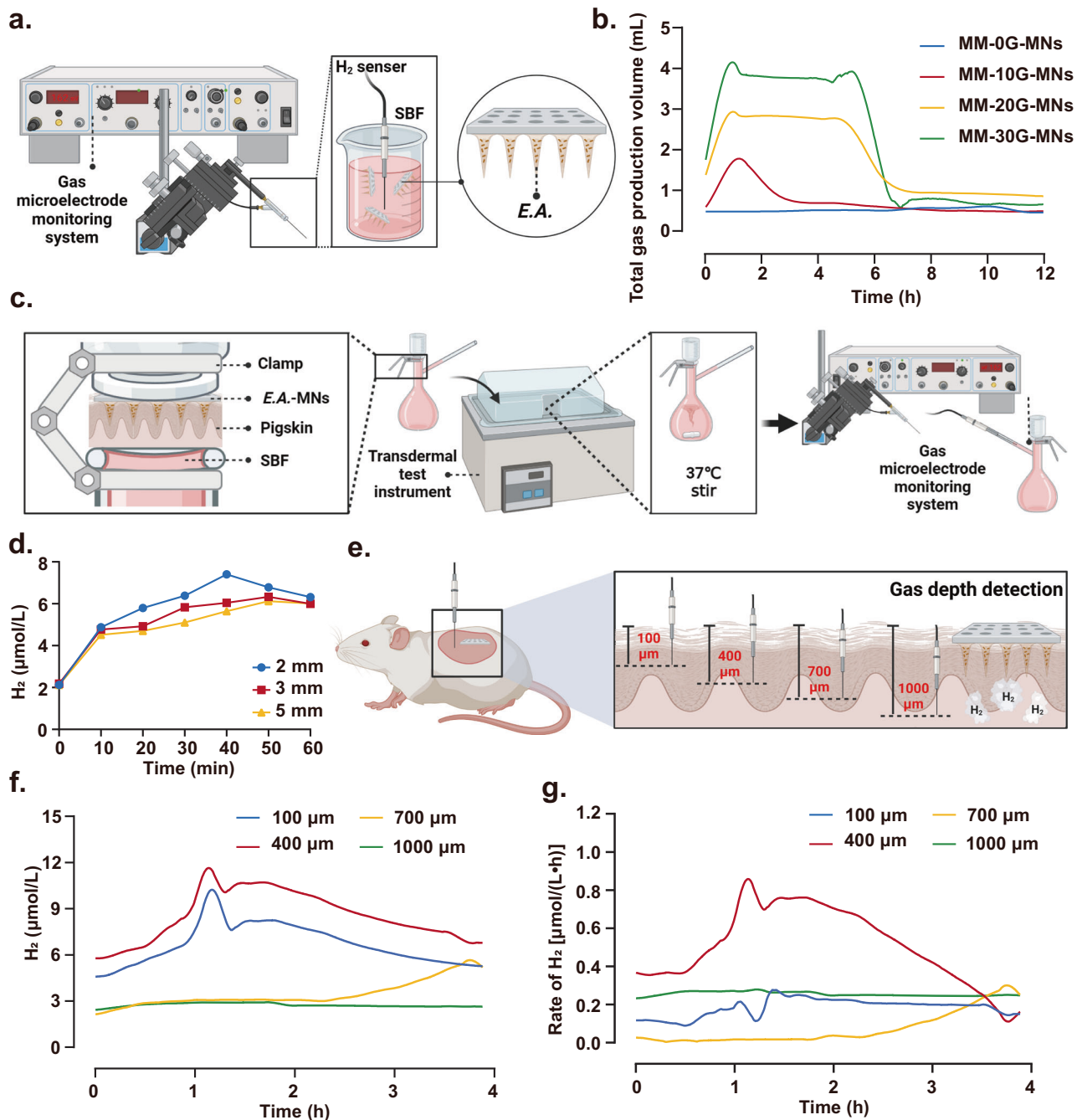
Fig. 4 | Characterization of gas penetration depth of microorganism micro-engine microneedles (MM-MNs). a Experimental diagram illustrating the detection of gas production from MM-MNs in simulated body fluids using a gas microelectrode system. Created with BioRender.com/e13d275. **b** Gas release from single microneedles loaded with different concentrations of glucose when immersed in simulated body fluid. **c** Test diagram of the penetration of MM-MNs through different skin thicknesses by using a transdermal test instrument. Created with BioRender.com/e13d275. **d** Trends in hydrogen gas concentration in simulated body fluid over time after penetrating different thicknesses of pig skin. Mean ± SD of $n = 3$ independent samples. **e** Experimental diagram of microelectrode real-time monitoring of subcutaneous gas concentrations at different depths. Created with BioRender.com/e13d275. **f, g** Trends in hydrogen gas concentration (**f**) and gas production rate (**g**) within the skin over time.

By comparing the digital microscope images (Fig. 3c) and scanning electron microscope images (Fig. 3e) of the microorganism micro-engine microneedles (MM-MNs) and empty microneedles (MNs), it can be observed that the surface morphology of the microneedles remains unchanged before and after microbial encapsulation. The puncture force of the microneedle tips was measured using a universal mechanical tester (Fig. 3d). The results showed that the encapsulation of microorganisms did not cause significant changes in the puncture force, which reached approximately 0.6 N, well

exceeding the force required for penetrating human skin. To validate the viability of microorganisms after encapsulation in the microneedles, we stained the MM-MNs with fluorescent dyes of Dry methylaluminoxane (DMAO) and Ethidium Homodimer III (EthD-III). The results of fluorescence microscopy (Fig. 3f and Supplementary Fig. S8) demonstrate that nearly all microorganisms maintained a high level of activity, with minimal occurrence of diseased cells. In addition, we tracked the activity of *E.A.* in microneedles over 48 h under room temperature (25 °C) and storage at 4 °C (Supplementary Figs. S9–S11).

The results showed that low temperatures could effectively extend the activity duration of *E.A.* in microneedles. However, even at room temperature (25 °C), *E.A.* maintained a considerable level of activity within the first 24 h.

We conducted layer-by-layer scanning of the loaded microneedles using confocal microscopy. In comparison to the positive control group subjected to sterilization treatment (Fig. 3g), the loaded microneedles exhibited a higher level of activity. In summary, the above data indicate that *E.A.* maintains a high activity during the preparation of microneedles. This provides the conditions for continuous gas production by active microorganisms in microneedles, forming the foundation for pneumatic motor microneedles.

Characterization of gas penetration depth of microorganism micro-engine microneedles (MM-MNs)

E.A. has been verified to maintain its activity within microneedles. However, for it to truly function as a pneumatic motor, the smooth release of gas from the microneedles is crucial. To quantitatively assess the gas production of MM-MNs and verify whether the duration and total amount of gas production can be controlled by adjusting the concentration of the loaded glucose substrate, we prepared microbial microneedles loaded with different concentrations of glucose: MM-MNs with 30 mg/mL glucose (MM-30G-MNs), MM-MNs with 20 mg/mL glucose (MM-20G-MNs), MM-MNs with 10 mg/mL glucose (MM-10G-MNs) and MM-0G-MNs. We selected one patch of microneedles and immersed them in simulated body fluid. The gas production was measured using an H_2 electrode probe (Fig. 4a). The results showed that the microbial microneedles loaded with 30 mg/mL of glucose had the most significant gas production duration and amount (Fig. 4b). In subsequent experiments when investigating the drug delivery performance and mechanism of the microbial microneedles, we defaulted to using 30 mg/mL as the substrate concentration when not otherwise specified (MM-MNs).

This indicates that *E.A.* not only maintains a high activity after encapsulation in the microneedles, but can still use the substrate retained in the microneedles and the surrounding to simulate glucose in body fluids to produce gas. To investigate the ability of gas produced by MM-MNs to penetrate the human epidermis effectively, we used H_2 as a detection indicator. We explored the penetration depth of gas generated by MM-MNs in human tissues.

First, we inserted MM-MNs into pigskin of varying thicknesses. We used a transdermal testing apparatus to measure the gas concentration that passed through the skin in simulated body fluid, reflecting the gas permeability of MM-MNs (Fig. 4c). The results revealed a gradual reduction in the quantity of penetrated gas with increasing thickness of the porcine skin (Fig. 4d). Even within porcine skin of 5 mm thickness, commendable penetration capability persisted, as the increase in skin thickness did not lead to a substantial decrease in gas permeation. Subsequently, we selected porcine skin with a thickness of 5 mm and introduced MM-MNs into it to simulate the process of gas generation within the skin. Employing H_2 microelectrodes, we monitored the temporal changes in H_2 concentrations at different depths beneath the skin tissue surface (ranging from 100 μm to 1000 μm) and the corresponding alterations in gas production rates (Fig. 4e–g). The dissolved H_2 concentration within the tissue indirectly reflected the overall mixed gas concentration within the tissue. The above data show that the gas generated by the loaded *E.A.* as a gas power source in the microneedles can penetrate the dermis to the depth of the skin tissue, and the deepest penetration can be more than 5 mm of the skin, providing a basis for its use as a power source to push drugs into the tissue.

Characterization of drug delivery performance of microorganism micro-engine microneedles (MM-MNs)

After verifying the performance of microbial pneumatic power, further validation is needed to determine whether double-layered microneedles can effectively propel the drug for enhanced release. This is crucial for assessing whether the drug's penetration ability into deeper tissues has been improved[22]. Next, we proceeded to validate the functionality of MM-MNs in drug release. To begin with, we substituted the pharmaceutical agent with rhodamine dye and simulated the drug release process in vitro. The preparation protocol entailed blending rhodamine with the soluble microneedle matrix material, polyvinyl alcohol (PVA), and subsequently casting it into molds for solidification. Following this, insoluble matrix materials, poly (ethylene glycol) diacrylate (PEGDA), with and without microbial inclusion, were introduced and solidified as a bilayer core-shell structured microneedle (Fig. 5a, b). To accomplish this, two distinct variations of microneedles were formulated: rhodamine-loaded MM-MNs (RMM-MNs) and rhodamine-loaded MNs (R-MNs). Initially, these two types of microneedles were separately introduced into the simulated physiological fluid at 37 °C. Over time, the absorbance of the released rhodamine dye into the simulated physiological fluid environment was quantified using ultraviolet spectrophotometry (Fig. 5c). It is evident that microbial aero-dynamic forces significantly contribute to drug release, facilitating the expedited dissolution of the outer PVA shell and the accelerated release of the pharmaceutical agent.

In order to verify whether the gas production and rate can be controlled indirectly by adjusting the concentration of glucose encapsulated in the microneedles to control the depth of the gas to push the dye through the skin, we conducted the following verification experiments. Four distinct variations of microneedles were formulated: rhodamine-loaded MM-MNs with 30 mg/mL glucose (RMM-30G-MNs), rhodamine-loaded MM-MNs with 20 mg/mL glucose (RMM-20G-MNs), rhodamine-loaded MM-MNs with 10 mg/mL glucose (RMM-10G-MNs) and rhodamine-loaded MNs (R-MNs). Subsequently, these four microneedle variants were inserted into equivalent porcine skin tissue. Following a 12 h incubation period, confocal microscopy was employed to observe the depth of dye penetration within the tissue (Fig. 5d, e). The results elucidate a notably enhanced depth of penetration of dye in the RMM-30G-MNs group, reaching up to about 900 μm beneath the skin, where gas-producing bacteria participated in the diffusion process. The aforementioned experiments employed dye to simulate drug release ex vivo. Quantitative analysis of fluorescence intensity at different subcutaneous depths in each group concluded that the impact of varying glucose substrate concentrations on drug diffusion depth and range is minimal within the 0-400 μm range (Fig. 5e). Significant differences only appear at depths greater than 500 μm, confirming that our designed microbial gas-engine-powered microneedles are controllable and can significantly increase drug delivery depth and range.

Moving forward, carpool (a clinical pharmaceutical agent used for psoriasis treatment) was employed in lieu of rhodamine dye within the microneedles (Fig. 5f). Consequently, two other sets of microneedles were generated: carpool-loaded MM-MNs (CMM-MNs) and carpool-loaded MNs (C-MNs). These two microneedle groups were inserted into the depilated dorsal region of BALB/c mice, and following a 12-hour period, the microneedles were retrieved, accompanied by the collection of dorsal skin and subcutaneous tissue samples. Subsequently, liquid chromatography was employed to ascertain the concentration of carpool within these samples (Fig. 5g, h and Supplementary Fig. S15). The outcomes distinctly demonstrate a heightened drug concentration within the subcutaneous tissue of the CMM-MNs group, thereby substantiating the capacity of these biomimetic microbial-aerodynamic microneedles to facilitate deep-tissue drug permeation within animal tissue. We also collected skin samples from mice in the CMM-MNs group at different time points to measure the drug retention in the epidermis and subcutaneous tissue. This verified that, over time, the drug gradually penetrated from the epidermis into the subcutaneous tissue along with the gas production process. It can also be concluded that the microbial microneedles we
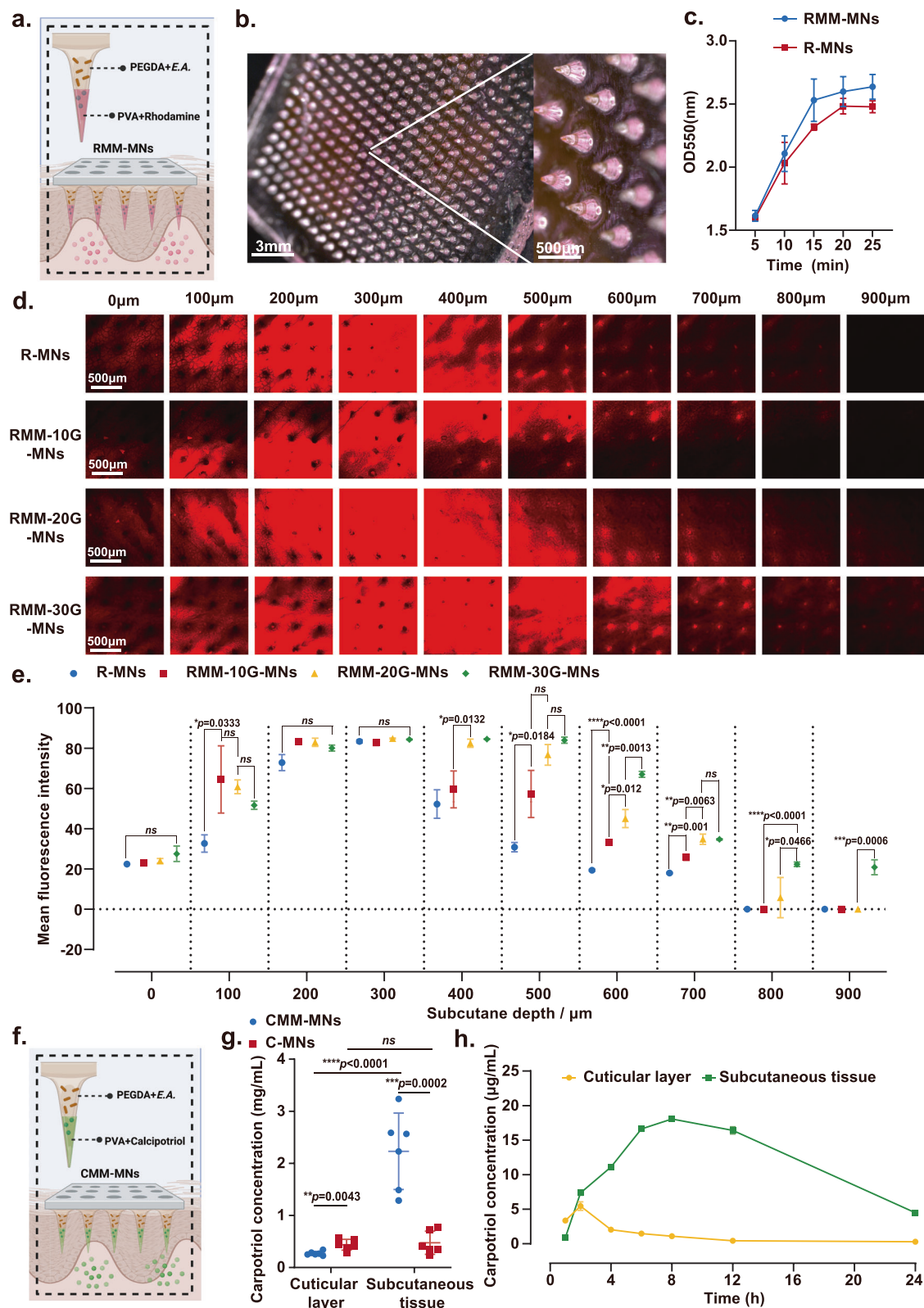
designed exhibit excellent transdermal efficiency and drug retention rates in vitro. The increase in penetration depth of microneedles drug delivery ensures that the drug is more effectively absorbed by the skin. This is particularly important for drugs requiring higher bioavailability, as it can reduce the required dosage and alleviate potential side effects. It provides a faster route for drug delivery, accelerating the onset of treatment, which is particularly beneficial in situations where rapid symptom relief is crucial.

The diffusion of drugs under the skin is controlled by the gas-producing behavior of microbial engines

Microbial microneedles powered by *E.A.* as the gas-producing engine have been proven to significantly improve transdermal drug delivery efficiency and increase the range and depth of drug diffusion. However, further verification is needed to understand how the micro-engine precisely controls the drug release behavior. To more accurately investigate the diffusion process and range of the drug within

Fig. 5 | Characterization of drug delivery performance of microorganism micro-engine microneedles (MM-MNs). a Double-layer microneedles with an outer layer loaded with Rhodamine dye and an inner layer containing Poly(ethylene glycol) diacrylate (PEGDA) loaded with *E.A.*. Created with BioRender.com/e13d275. **b** Digital microscope image of RMM-MNS. Scale bar, 3 mm (Left); 500 µm (Right). **c** The release of rhodamine over time in simulated body fluid. Mean ± SD of $n = 3$ independent samples. **d** Confocal microscopy imaging of the penetration depth of Rhodamine dye released by microneedles loaded with different concentrations of glucose into the skin. Scale bar, 500 µm. **e** Fluorescence intensity of Rhodamine dye diffusion at different depths beneath the skin released by microneedles loaded with varying concentrations of glucose. Mean ± SD of $n = 3$ independent samples. Two-sided Student's *t* test. **f** Double-layer microneedles with an outer layer loaded with Calcipotriol and an inner layer containing PEGDA loaded with *E.A.*. Created with BioRender.com/e13d275. **g** Determination of the concentration of Carpotriol in the skin's surface and subcutaneous tissue by high-performance liquid Chromatography (HPLC). Mean ± SD of $n = 6$ independent samples. Two-sided Student's *t* test. **h** Changes in caprotriol concentration in skin surface and subcutaneous tissue over time as determined by HPLC. Mean ± SD of $n = 6$ independent samples. Two-sided Student's *t* test. A representative image of four biologically independent samples from each group is shown in (**b**) and (**d**).

the skin, we set up an observation period of 24 h. During this period, we observed the time-dependent release of a dye simulating the drug subcutaneously and conducted a quantitative evaluation of the fluorescence intensity (Fig. 6a–c and Supplementary Fig. S16). Firstly, it is evident that in the shallower epidermal layers (0–400 µm), the drug can diffuse extensively within 1-2 h. This can be attributed to the larger volume at the base of the conical microneedles, which contain more gas-producing microorganisms. After 4 h, the fluorescence range in the deeper skin tissues (500–600 µm) begins to expand. Between 6 and 8 h, the drug can diffuse into deeper tissues (>700 µm). As the observation period extends to 24 h, the diffusion depth of the drug can further increase, likely due to the ongoing molecular diffusion and thermal motion of the drug or dye molecules. To verify that this drug diffusion behavior is closely related to *E.A.* gas production, we compared the time-dependent gas production curve of the microneedles with the diffusion curves of the dye at various subcutaneous depths (Fig. 6d). It is clear that as the total amount of gas increases during the gas production process, the drug begins to diffuse in the superficial layers of the skin at the same time. The diffusion of the drug in the deeper layers shows a delay of about 1-2 h as it gradually increases with subcutaneous depth, indicating that the gas-driven drug diffusion takes time. However, it can still be concluded that the gas production process of *E.A.* is highly correlated with drug diffusion.

The microneedle matrix encapsulating *E.A.* is made of cured PEGDA, while the outer layer encapsulating the drug/dye is made of PVA. These two media have different densities. When the gas released by *E.A.* reaches the interface between the two media, it inevitably causes a change in pressure. Generally speaking, gas pressure is produced by the frequent and continuous collisions of a large number of molecules undergoing random thermal motion against the walls of the container. The impact of a single molecule colliding with the wall is brief, but the frequent collisions of many molecules with the wall create a continuous and uniform pressure. Therefore, from the perspective of molecular kinetic theory, gas pressure is the average force exerted by a large number of gas molecules on the unit area of the container wall.

Treatment of psoriasis using microorganism micro-engine microneedles (MM-MNs)

Among various clinical applications, we tested microbial pneumatics microneedles for transdermal delivery of calcipotriol to treat psoriasis. Psoriasis is a genetically and immunologically mediated inflammatory skin disease whose treatment primarily relies on symptom control[23]. Current treatment methods include local therapy and systemic therapy. Systemic therapy has many limitations, such as hepatic first-pass metabolism, hepatotoxicity, gastrointestinal disturbances, needle pain, and phobia, and it requires administration by healthcare professionals. On the other hand, local treatment for mild to moderate psoriasis faces challenges such as poor skin permeability, short drug retention time, greasy topical vehicles, and lack of controlled release.

Microneedles, as a novel transdermal delivery method, bypass the skin barrier and enhance direct drug penetration into the skin, addressing the limitations of traditional transdermal drug delivery systems. However, due to the limited length of the needle shaft, they cannot penetrate the thickened epidermis, thus reducing the transdermal diffusion efficiency of drugs. Therefore, we chose psoriasis as the disease model to evaluate the effectiveness of microbial biomimetic pneumatics microneedles in clinical therapy. We used the imiquimod (IMQ)-induced psoriasis mice model, which can reproduce typical clinical symptoms and pathological features of human psoriasis, making it a feasible animal model for studying psoriasis (Fig. 7a).

We evaluated the progression of psoriatic lesions on the mice's back, including modeling efficacy and treatment efficacy, using the Psoriasis Area and Severity Index (PASI) score based on four dimensions: erythema, scaling, thickness, and skin lesion severity. We established five experimental groups: the modeled untreated group (Control), the calcipotriol treatment group (Calcipotriol), the calcipotriol-loaded microneedles group (C-MNs), the calcipotriol-loaded MM-MNs group (CMM-MNs), and the MM-MNs group (MM-MNs).

Throughout the modeling and treatment process, we recorded the PASI scores of the mice back (Fig. 7b and Supplementary Figs. S17, S18) and observed the skin appearance of the back (Fig. 7i and Supplementary Fig. S19). We found that the CMM-MNs group had the best treatment efficacy and the fastest improvement in disease progression. In addition, we conducted tests on psoriasis-related inflammatory factors in each group, and the results (Fig. 7c–h) confirmed the relevant data regarding treatment efficacy, with the CMM-MNs group having the lowest levels of inflammatory factors. By observing skin tissue sections stained with hematoxylin and eosin (H&E) (Supplementary Fig. S20a), we observed a significant improvement in inflammatory cell infiltration and a reduction in skin epidermal thickening in the CMM-MNs group. Furthermore, the results of H&E-stained liver and kidney tissue sections, inflammatory factor data in the control group, and cytotoxicity tests showed that microbial pneumatics microneedles did not exhibit significant hepatotoxicity, nephrotoxicity, or cytotoxicity, indicating their potential for clinical application (Supplementary Fig. S20b–d).

However, the IMQ-induced psoriasis animal model is an acute induction model characterized by acute inflammatory responses, and thus cannot fully replicate the chronic inflammatory state of psoriasis. In pharmacological studies, cessation of IMQ can alleviate symptoms in psoriatic mice. To better simulate the chronic inflammatory state of psoriasis, we also employed a second modeling method, namely therapeutic intervention under continuous IMQ induction conditions (Fig. 8a). In the continuous IMQ-induced mouse model, the disease progression continues to worsen, but significant improvements in the scaling, redness, and inflammation factor levels, as well as a notable reduction in skin thickness, were observed in the CMM-MNs group (Fig. 8b–k). In conclusion, microbial pneumatics microneedles demonstrated effective treatment of psoriasis through transdermal delivery of calcipotriol, offering potential clinical value in improving the condition and reducing inflammation response. At the same time, we observed an interesting phenomenon: in the MM-MNs group without drug loading, a relatively noticeable therapeutic effect was observed in the first non-sustained modeling experiment. The amount of skin scaling on the backs of the mice was significantly reduced, and there was also a significant difference in the reduction of inflammatory
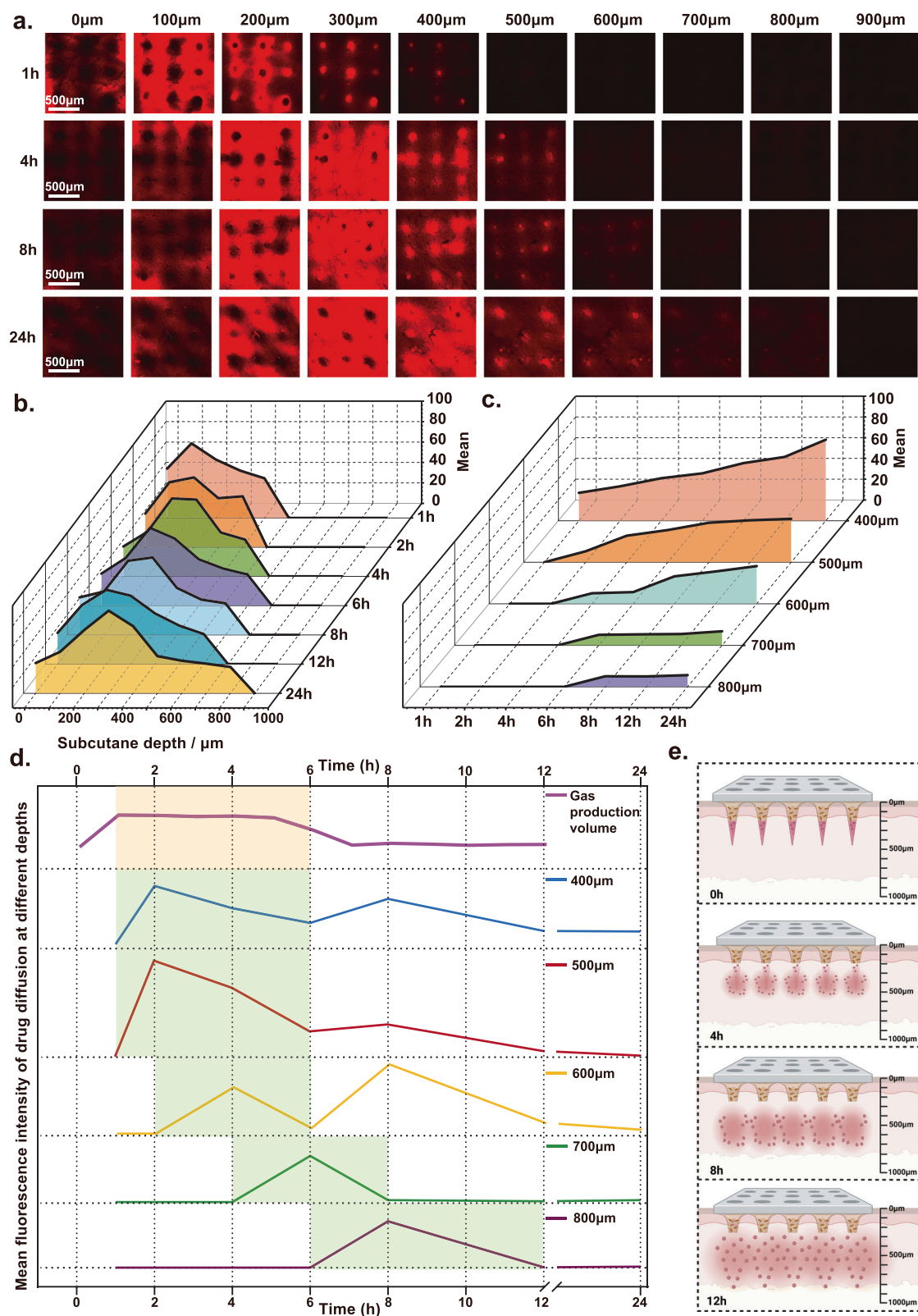
Fig. 6 | The diffusion of drugs under the skin is controlled by the gas-producing behavior of microbial engines. a Confocal microscopy imaging of the release and diffusion over time of dye-simulated drugs at different depths beneath the skin. Scale bar, 500 μm. **b**, **c** The average fluorescence intensity of dye-simulated drugs diffusing over time at different depths beneath the skin. **d** The curves show the average fluorescence intensity of drug diffusion over time at different depths, and the curves depict gas production by microneedles over time. **e** A schematic diagram illustrating the gradual dissolution and diffusion of dye-simulated drugs under the skin due to gas production by microneedles, penetrating into deeper tissues. Created with BioRender.com/u33l993. A representative image of four biologically independent samples from each group is shown in (**a**).
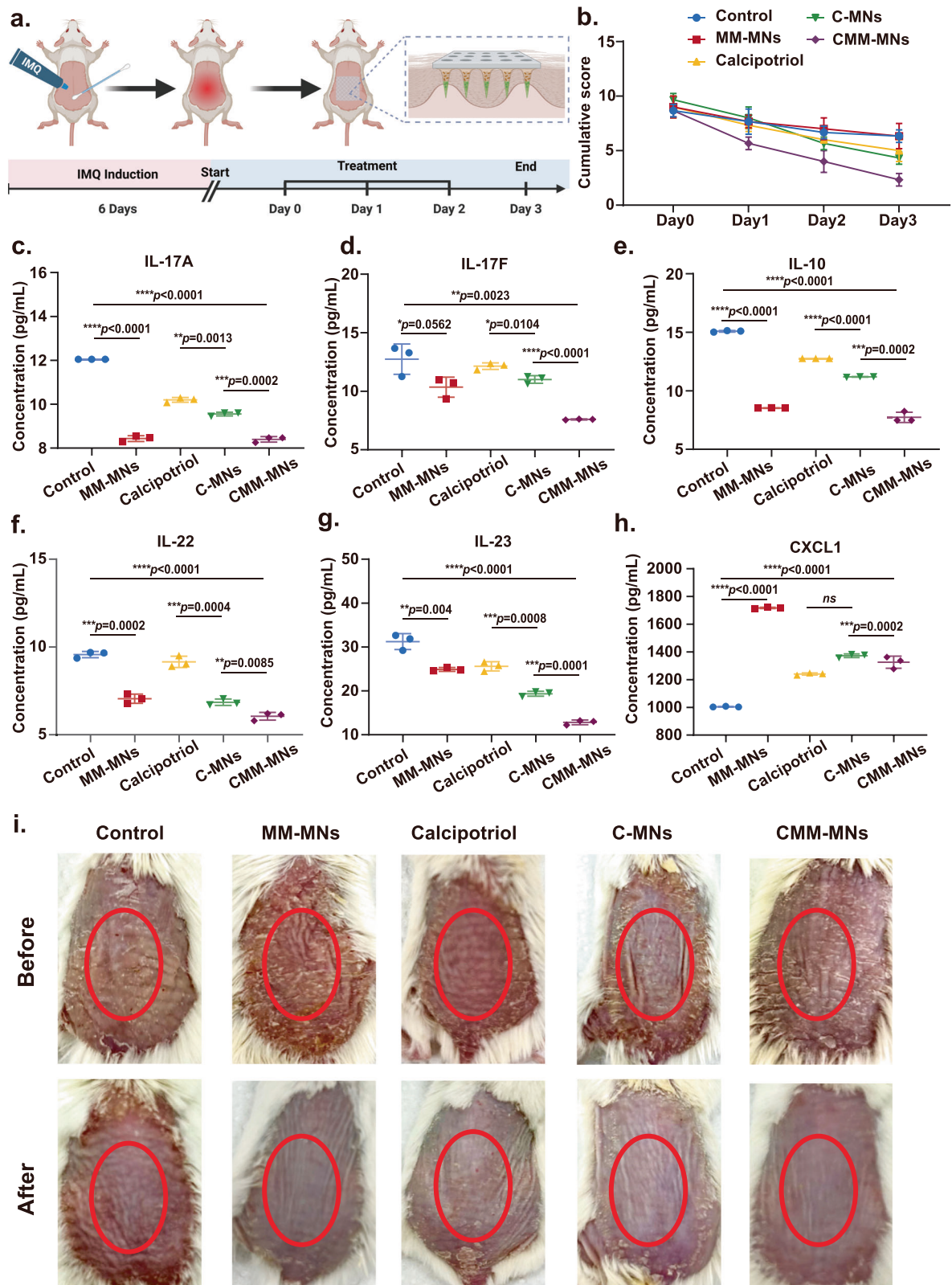
Fig. 7 | The therapeutic efficacy of microorganism micro-engine microneedles (MM-MNs) for psoriasis treatment. a Establishment of the animal model and treatment procedure. Created with BioRender.com/u33l993. **b** Changes in PASI scores during the treatment process. Mean ± SD of *n* = 3 independent samples. **c**–**h** ELISA experiment to measure the levels of psoriasis-related inflammatory factors. (**c**): IL-17A; (**d**): IL-17F; (**e**): IL-10; (**f**): IL-22; (**g**): IL-23; (**h**): CXCL1; (**c**–**h**) mean ± SD of *n* = 3 independent samples. Two-sided Student's *t* test. **i** Changes in the condition of the back of mice during the treatment process. A representative image of three biologically independent samples from each group is shown in (**i**).
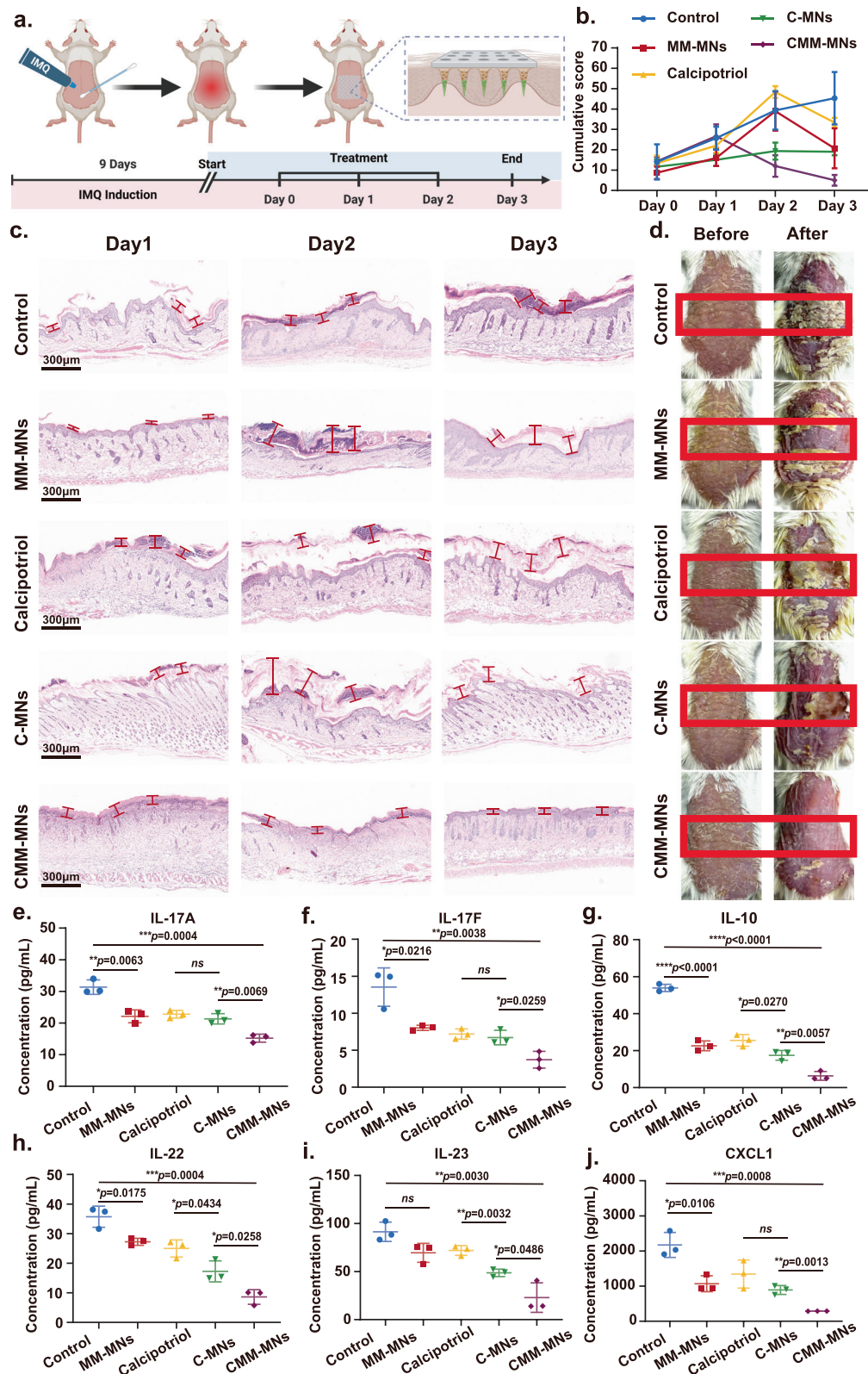
Fig. 8 | The therapeutic efficacy of microorganism micro-engine microneedles (MM-MNs) for chronic psoriasis treatment. a Establishment of the animal model and treatment procedure. Created with BioRender.com/u33l993. **b** Changes in PASI scores during the treatment process. Mean ± SD of *n* = 3 independent samples. **c** H&E staining results of the back skin in each group. Scale bar, 300 μm. **d** Changes in the condition of the back of mice during the treatment process. **e**–**j** ELISA experiment to measure the levels of psoriasis-related inflammatory factors. (**e**): IL-17A; (**f**): IL-17F; (**g**): IL-10; (**h**): IL-22; (**i**): IL-23; (**j**): CXCL1; **e**–**j** mean ± SD of *n* = 3 independent samples. Two-sided Student's *t* test. A representative image of three biologically independent samples from each group is shown in (**c**) and (**d**).

factors compared to the control group (Fig. 7c–i). This suggests that in the non-sustained psoriasis model, the gas produced by the active microorganisms in the microneedles also has a clear therapeutic effect. This observation led us to hypothesize that certain components of this gas might also help alleviate the inflammation associated with psoriasis, which shifted our focus to H_2. Hydrogen (H_2), as a molecule with strong antioxidant and anti-inflammatory properties, has shown potential therapeutic effects in various diseases in recent years[24]. For immune-mediated diseases like psoriasis, oxidative stress, and inflammatory responses are key factors in the pathological process. We speculate that H_2 could alleviate psoriasis symptoms by reducing oxidative stress, thereby inhibiting the overactivation of inflammatory signaling pathways[19]. However, in the group subjected to continuous IMQ modeling, the therapeutic effect was significantly weakened and was limited to the skin area treated with microneedles. We believe this can be explained by the fact that psoriasis is an immune-mediated skin disease, with its pathological characteristics mainly reflected in the dysregulation of immune cells within the dermis. The activity of these immune cells in the dermis leads to local inflammation, accelerated proliferation of keratinocytes, and the formation of typical psoriatic plaques. The application of H_2 alone only alleviated inflammation in the epidermis and did not impact the immune cells in the dermis. Therefore, in the continuous modeling animal model, where the disease continues to worsen, systemic therapeutic effects could not be achieved. However, for the CMM-MNs group, H_2 can assist in deep drug delivery treatment, achieving a combined therapeutic effect. This unexpected coincidence greatly enhances the application efficacy of microbial microengineered microneedles.

Discussion

We propose a living microneedle micro-engine system with an adjustable propelling force that harnesses gas-producing microorganisms internally loaded to generate powerful gas dynamics. This system propels drug dissolution and release beneath the skin, enhancing the depth, diffusion range, and efficiency of transdermal drug delivery via microneedles. The microneedles, fabricated with PEGDA as the matrix, encapsulate *Enterobacter Aerogenes (E.A.)* and exhibit superior characteristics in sustained gas generation, total gas production, and instantaneous release rate when compared to metallic substrates. These microbes maintain excellent biological activity for several hours after formation. The continuous gas propulsion force generated by these microorganisms can reach over 0.04 N, enabling the drug to achieve a maximum transdermal depth of up to 1000 µm in the skin. Compared to conventional microneedles relying on free diffusion for drug delivery, the drug delivery depth achieved by the living microbial pneumatic microneedle micro-engine system can be increased to more than 200%. In addition, the encapsulated microbes within the insoluble microneedle matrix material remain confined within the microneedles without release, isolating them from epidermal tissue cells. This isolation helps prevent toxicological tissue damage, ensuring biocompatibility. In a mice model of psoriasis, significant improvement in overall symptoms was observed by delivering the drug calcipotriol using pneumatic-active microneedles. In summary, the biologically active microbial-driven microneedle micro-engine described in this study offers possibilities for treating deep tissue lesions, providing a creative paradigm for controlled microneedle drug delivery. This technology has unique advantages, including ease of scalable production, prolonged biological activity, deep skin tissue penetration, and biocompatibility. Its broad applicability makes it suitable for various diseases and drugs.

In the gas-assisted drug delivery system, the dynamics of gas diffusion and pressure distribution in the skin microenvironment play a critical role. Specifically, after the gas is injected into the subcutaneous tissue, gas molecules begin to diffuse through the tissue according to Fick's laws of diffusion[25]. The diffusion process is influenced by the structure and composition of the skin, including the stratum corneum, epidermis, and dermis. As observed in our experiments, gas diffusion in the skin exhibits significant lateral diffusion characteristics. This indicates that gas diffuses not only longitudinally (in-depth) but also laterally (in-plane). When gas diffuses subcutaneously, it creates a high-pressure environment in the local area. This pressure can be explained by the volume expansion of the gas and the limited compressibility of skin tissue. According to the ideal gas law, when gas is released in an enclosed or semi-enclosed space (such as subcutaneous tissue), its volume expansion exerts pressure on the surrounding tissue. This pressure acts as a "push" for the drug in the microneedle delivery system, facilitating the drug's penetration into deeper layers of tissue. As mentioned in our previous experimental results, despite the presence of lateral gas diffusion, the local high-pressure area formed around the microneedle puncture point enables the drug to effectively diffuse longitudinally into deeper layers. By controlling the glucose concentration loaded in the microneedles, we can adjust the speed and pressure of gas release, thereby controlling the depth and range of drug diffusion (Fig. 5d, e). The porous structure and complex physiological characteristics of the skin microenvironment make gas diffusion and pressure application somewhat predictable and controllable. By combining Darcy's Law[26] and Fick's Law, it is theoretically possible to establish a mathematical model for gas and drug diffusion to further understand the pressure effects of gas on drug delivery. This is also a direction worth investing more efforts in the future exploration of gas-driven microneedles.

Although some microbes have been used as Micro-engine for drug delivery. Researchers have used the autonomous movement of algae to design micro-robots that can stay in the gastrointestinal tract[27]. However, in transdermal therapy, due to safety concerns and the inherent nature of microorganisms, it is not feasible to use the microorganisms themselves directly within tissues as power micro-engines. Therefore, it is necessary to indirectly harness their gas production capacity. The reaction conditions for active microorganisms are mild, and the substrates required for gas production are often simple nutrients like glucose, making them more compatible with living organisms. They can sustain gas production continuously and at a low cost. If the gas-producing microorganisms can be cleverly combined with the transdermal drug delivery method using microneedles, it could bring insights to the field of microneedle-controlled drug delivery. In comparison to gas-producing materials[28], active microorganisms with gas-producing capabilities are undoubtedly a better choice[29].

For future research, it will be necessary to explore in greater detail the physical model of gas diffusion from the microneedle pores and the propulsion of outer-layer drugs into deeper tissues. In addition, it will be important to quantitatively determine the contributions of factors such as gas propulsion force and microneedle length to drug delivery. This will provide theoretical support for subsequent microneedle-related studies. In addition, for drugs of different molecular weights, including high-molecular-weight drugs such as proteins[30] and cell therapies, further investigation is needed to determine whether microbial-driven microneedles can provide sufficient propulsion for their diffusion, thereby expanding their application in other clinical settings[31]. Future research can also expand the range of microbial species encapsulated in the microneedles and analyze the composition of mixed gases[32], allowing them not only to serve as a source of propulsion but also to utilize therapeutic gases with beneficial effects, such as H_2[33], NO[34], NH_3 and H_2S[35], which may synergize with loaded drugs. Looking ahead, gaining a more accurate understanding of how microbiota-driven pneumatic microneedles interact with the extracellular matrix microenvironment obtaining necessary nutrients and gas substrates will be an interesting research direction to further enhance gas production time and efficiency within the microneedles[36]. If the components within the extracellular matrix microenvironment, altered by diseases[37–46], can be effectively utilized,

the design of microenvironment-responsive living microbial aerodynamic microneedles could be considered[47]. Previous studies have demonstrated the application of responsive micro-needles prepared by combining environment-responsive materials with micro-needles in various diseases[48]. For example, in the application of microneedles for metabolic diseases such as diabetes, the amount and rate of microneedle release of anti-sugar drugs such as insulin can be regulated by designing microbial gas-producing micro-engines with different parameters according to the change of glucose concentration in the tissue microenvironment[49,50]. In the future, the design of microneedles with physiological elements of microorganisms that can be influenced by changes in the microenvironment may also be considered[51]. In conclusion, the microorganism microneedle microengine we developed provides a creative paradigm for the penetration and diffusion of drugs into deep tissues and can be incorporated with advanced biomedicine[52-54].

Methods

Cells
HaCaT keratinocytes (provided from the SUNNCELL, Wuhan, China) were cultured in Dulbecco's modified Eagle's medium(DMEM; Gibco, USA) containing 10% heat-inactivated fetal bovine serum (FBS; Gibco) and 1% penicillin and streptomycin (P/S; Gibco). Cells were incubated at 37 °C under a 5% CO_2 atmosphere.

Material
Polyethylene glycol diacrylate (PEGDA, average Mw = 700), 2-hydroxy-2-methylpropiophenone (HMPP), Rhodamine B, polyvinyl alcohol (PVA), and caprylic triglyceride were purchased from HEOWNS Company. *Enterobacter Aerogenes ATCC 13048*(*E.A.*) was obtained from Solarbio. Male *BALB/c* mice (6–8 weeks old, 18–22 g) were strictly handled in accordance with the Animal Management Regulations of Tianjin, China. All animal experiments in this study were approved by the Tianjin Medical University School of Medicine.

GC Analysis of gas produced by *E.A.*
A certain amount of gas produced by *E.A.* was collected. Component analysis was carried out using a gas chromatograph (Agilent 7890B). The testing conditions were as follows:

Column:
1. Agilent 25 m HP-AS/L + 2 m DB-1 (0.320 mm) (− 60 °C–200 °C) (27 m × 320 μm × 8 μm)
2. Agilent 0.4 m × 1/8 HaySep A 80/100 UM 25 mm (0 °C–165 °C)
3. 5Ft HayeSepA 80/100 + 7Ft MS5A 60/80 (0 °C–165 °C)
4. Agilent 3Ft × 1/8 HayeSep Q 80/100 UM (0 °C–275 °C)
5. 8Ft × 1/8 MolSieve 5A 60/80 UM (0 °C–400 °C)

Injector: Split/Splitless inlet, injector temperature 120 °C
Detector: FID (Flame Ionization Detector) at 300 °C; TCD2 at 250 °C; TCD3 at 250 °C
Column Oven Temperature: Initial temperature 60 °C, equilibration time 0.5 min, maximum column oven temperature 190 °C.

Exploration of optimal gas production conditions for *E.A.*
We conducted tests for the effect of *E.A.* inoculation levels, substrate concentrations, and random time on gas production by *E.A.*, as per the table below, and recorded the results in graphs. Then we used UV spectrophotometer(Thermo scientific Evolution 220) to detect the absorbance of different culture groups with OD of 660 nm, so as to judge the growth of *E.A.* Substrate concentration: 0, 10, 20, and 30 mg/mL; Inoculum: 0.05, 0.10, 0.20, 0.40%; Culture time: 3, 6, 12, 24 h.

The hydrogen electrode detects gas production
Use the Danish UNISENSE microelectrode system H_2-25 model to detect the gas production of *E.A.* under different substrate concentrations. Undersealed conditions at a water bath temperature of 37 °C, *E.A.* was cultured for 12 h under different substrate concentrations (0, 10, 20, 30 mg/mL) while microelectrodes were continuously measured for 12 h. When measuring subcutaneous gas concentration, the electrode was inserted subcutaneously.

Preparation method of single-layer bacteria-carrying microneedles
First, a solution was prepared by mixing PEGDA and anhydrous ethanol in a 7:3 ratio to make a 10 mL solution. Then, 100 μL of HMPP (1%, v/v) was added to the solution, and it was thoroughly mixed to obtain the substrate solution. Next, a solution of *Enterobacter Aerogenes ATCC 13048(E.A.)* was placed in a centrifuge tube, and the centrifuge was set to 3000 rpm for 15 min. The resulting centrifuged pellet was thoroughly mixed with the substrate solution to obtain a bacteria-loaded substrate material. Different proportions of glucose solution can be added to the substrate solution as needed to obtain microneedle patches with varying substrate concentrations. Subsequently, a microneedle fabrication mold (microneedle width 200 μm, needle length 500 μm) was taken, and 300 μL of the bacteria-loaded substrate material was added to it. The mold was placed in a vacuum pump for 20 seconds to remove any bubbles from the microneedle mold's needle array. The mold was then removed, and if necessary, it was exposed to a UV lamp(LUYOR-3109, 27w LED lamp) for 5 s to cure, resulting in complete microneedles. If there was any remaining liquid not drawn into the mold's pores, an additional 300 μL of the substrate solution was added to fill the mold. A UV lamp was used to cure it for 5 s, and the microneedles were demolded to prepare complete bacteria-loaded microneedles.

Preparation method of microorganism micro-engine microneedles (MM-MNs)
On the basis of preparing a single-layer microneedle, pre-add 100 μL of a mixture of PVA and rhodamine B/carbopol in the microneedle mold. After natural air-drying for 6 h, repeat the steps for making a single-layer microneedle by adding a bacterial-carrying solution based on PEGDA and curing it using ultraviolet irradiation.

Mechanical properties of MM-MNs
The mechanical performance of the bacteria-loaded microneedles was measured using a displacement force testing system (CMT6103, manufactured by MTS - Mechanical Testing Systems). This was done to assess the mechanical strength of the bacteria-loaded microneedles under compression. A single microneedle was attached to a vertically positioned rigid stainless steel platform (needle tip facing upwards). Then, the sensor probe of the testing system was lowered at a speed of 0.2 mm/s in the vertical direction toward the microneedles. Force measurement began when the sensor first made contact with the tip of the microneedle and continued until the sensor had moved 0.3 mm from the tip to the back of the patch.

Verification of bacteria-carrying microneedle activity
The Live & Dead Bacterial Staining Kit (YENSEN) was used to assess the viability of bacteria in the bacteria-loaded microneedles. The kit includes two fluorescent dyes, DMAO and EthD-III, which can respectively stain live bacteria in green and dead bacteria in red. DMAO is a green nucleic acid fluorescent dye that can stain both live and dead bacteria. EthD-III is a red nucleic acid fluorescent dye that selectively stains dead bacteria with damaged cell membranes. When DMAO and EthD-III are mixed for staining, bacteria with intact cell membranes exhibit green fluorescence, while bacteria with damaged cell membranes show both green and red fluorescence. The results were detected using fluorescence microscopy and confocal microscopy. The spectral characteristics are as follows: DMAO - Ex/Em = 503/530 nm (with DNA); EthD-III - Ex/Em = 530/620 nm (with DNA).

Physiological dissolution experiment

Rhodamine was mixed with the substrate material, and molds were used to create two sets of microneedles: one set loaded with Rhodamine (RMM-MNs) and another set without Rhodamine (R-MNs). These two types of microneedles were then placed in simulated physiological fluid at 37 °C. Every 10 min, a sample of the liquid was taken and placed in a measurement vessel. The absorbance at 550 nm was measured using UV-visible spectrophotometry.

Skin permeation test

Fresh pigskin was placed in a culture dish with the stratum corneum facing upwards, and ultrapure water was added to the culture dish to keep the pigskin moist but not submerged. Two sets of microneedles, one loaded with Rhodamine (RMM-MNs) and the other without Rhodamine (R-MNs), were inserted into the pigskin. After pressing them tightly for 24 h, the penetration depth of Rhodamine into the tissue was observed using a confocal microscope.

The retention of Calcipotriol in skin tissue measured by high-performance liquid chromatography (HPLC)

The pig skin or excised rat dorsal skin tissue was ground and extracted using ethanol. The extract was then analyzed using high-performance liquid chromatography (HPLC). The chromatographic column used was an Agilent Poroshell 120 EC-C18 column, with a column temperature of 35 °C and a flow rate of 1.0 mL/min. The mobile phase consisted of acetonitrile, methanol, and 0.01 mol/L phosphate buffer (pH 6.0 ± 0.1) in a ratio of 20:50:30. The detection wavelength was set at 264 nm.

The process of establishing a cellular inflammation model

Select well-growing cells, synchronize them in serum-free medium for 6 hours, and then induce them with TNF-α for 24 hours (TNF-α 20 μg/L).

Animal experiment

A 3 cm x 5 cm central area on the backs of mice was depilated, and a mild depilatory cream was used to remove surface hair. The mice were randomly divided into six groups. Five of the groups were administered 5% Imiquimod (62.5 mg) daily to the depilated area, and one group served as the non-model (healthy) group and was administered an equivalent amount of Vaseline ointment. During the modeling period, the severity of skin inflammation on the backs of the mice was assessed based on the PASI scoring criteria. The PASI scoring criteria were as follows: The severity of skin inflammation, including skin thickness, scale, and erythema, was assessed daily. Scores were assigned on a 5-point scale (0–4) for each parameter, and the total score was calculated as the sum of the scores for skin thickness, scale, and erythema.

Grouping of animal experiments

The five groups of psoriasis model mice were as follows: the untreated model group (Control), the calcipotriol treatment group (Calcipotriol), the calcipotriol microneedle group (C-MNs), the calcipotriol-loaded MM-MNs group (CMM-MNs), and the MM-MNs group (MM-MNs). Each group received the following treatments daily for three consecutive days: no treatment, subcutaneous injection of calcipotriol (dose), C-MNs treatment, treatment with calcipotriol-loaded MM-MNs, and MM-MNs treatment. During the treatment period, the severity of skin inflammation on the backs of the mice was also assessed based on the PASI scoring criteria. All animal experiments conducted in this work received approval from the animal tissue ethics committee of Tianjin University.

Detection of psoriasis-related inflammatory factors

After the treatment process, blood samples were collected from the periorbital venous plexus, with 3 mL obtained from each group. EDTA and heparin were added to provide anticoagulation. Subsequently, the samples were centrifuged at 3000 rpm for 30 min using a centrifuge, and the supernatant was collected and preserved. ELISA kits were then used to measure the expression levels of inflammatory factors, including IL-17A, IL-17F, IL-22, IL-23, IL-10, and CXCL1, in each group. After the procedure was completed, the absorbance (OD value) was determined at a wavelength of 450 nm using a microplate reader (BIOTEK H1M, USA), and sample concentrations were calculated.

Hematoxylin and eosin (H&E) staining

Hematoxylin and eosin (H&E) staining was performed on the microneedle (MNs) application sites. After the conclusion of animal experiments, a histopathological evaluation was conducted. Mice from each group were euthanized, and their hearts, livers, spleens, lungs, kidneys, and skin tissues where microneedles (MNs) were used were dissected and fixed in 4% formaldehyde solution. The fixed tissues were dehydrated with ethanol, embedded in paraffin, sectioned using a microtome, and analyzed following staining with hematoxylin and eosin (H&E).

Statistical information

All experimental results were expressed as means ± SD. A two-sided Student's *t* test was used for unpaired data. The other data were analyzed using the GraphPad Prism 8.0.2 software. *P*-values < 0.05 were considered significant.

Reporting summary

Further information on research design is available in the Nature Portfolio Reporting Summary linked to this article.

Data availability

All data supporting the findings of this study are available within the article and its supplementary files. Any additional requests for information can be directed to and will be fulfilled by the corresponding authors. Source data are provided in this paper.

References

1. Chen, Z. et al. Bioorthogonal catalytic patch. *Nat. Nanotechnol.* **16**, 933–941 (2021).
2. Gao, X., Li, J., Li, J., Zhang, M. & Xu, J. Pain-free oral delivery of biologic drugs using intestinal peristalsis–actuated microneedle robots. *Sci. Adv.* **10**, eadj7067 (2024).
3. Tran, K. T. M. et al. Transdermal microneedles for the programmable burst release of multiple vaccine payloads. *Nat. Biomed. Eng.* **5**, 998–1007 (2021).
4. Yang, B., Kong, J. & Fang, X. Programmable CRISPR-Cas9 microneedle patch for long-term capture and real-time monitoring of universal cell-free DNA. *Nat. Commun.* **13**, 3999 (2022).
5. Zhang, Y. et al. Scarless wound healing programmed by core-shell microneedles. *Nat. Commun.* **14**, 3431 (2023).
6. Sang, M. et al. Fluorescent-based biodegradable microneedle sensor array for tether-free continuous glucose monitoring with smartphone application. *Sci. Adv.* **9**, eadh1765 (2023).
7. Kusama, S. et al. Transdermal electroosmotic flow generated by a porous microneedle array patch. *Nat. Commun.* **12**, 658 (2021).
8. Chen, W. et al. Microneedle-array patches loaded with dual mineralized protein/peptide particles for type 2 diabetes therapy. *Nat. Commun.* **8**, 1777 (2017).
9. He, G. et al. Synthetic biology-instructed transdermal microneedle patch for traceable photodynamic therapy. *Nat. Commun.* **13**, 6238 (2022).
10. Kim, H. et al. Skin preparation–free, stretchable microneedle adhesive patches for reliable electrophysiological sensing and exoskeleton robot control. *Sci. Adv.* **10**, eadk5260 (2024).
11. Lin, K. et al. Mechanism-based design of agents that selectively target drug-resistant glioma. *Science* **377**, 502–511 (2022).

12. Meng, J. et al. A multistage assembly/disassembly strategy for tumor-targeted CO delivery. *Sci. Adv.* **6**, eaba1362 (2020).

13. Yu, L., Hu, P. & Chen, Y. Gas-generating nanoplatforms: Material chemistry, multifunctionality, and gas therapy. *Adv. Mater.* **30**, 1801964 (2018).

14. Liu, P. et al. Microneedle patches with O_2 propellant for deeply and fast delivering photosensitizers: Towards improved photodynamic therapy. *Adv. Sci.* **9**, 2202591 (2022).

15. Zhao, P. et al. Local generation of hydrogen for enhanced photo-thermal therapy. *Nat. Commun.* **9**, 4241 (2018).

16. Wang, D. et al. A mesoporous nanoenzyme derived from metal–organic frameworks with endogenous oxygen generation to alleviate tumor hypoxia for significantly enhanced photodynamic therapy. *Adv. Mater.* **31**, 1901893 (2019).

17. Chen, S. et al. Local H_2 release remodels senescence micro-environment for improved repair of injured bone. *Nat. Commun.* **14**, 7783 (2023).

18. Griffiths, C. E. M., Armstrong, A. W., Gudjonsson, J. E. & Barker, J. N. W. N. Psoriasis. *Lancet* **397**, 1301–1315 (2021).

19. Greb, J. E. et al. Psoriasis. *Nat. Rev. Dis. Prim.* **2**, 16082 (2016).

20. Shaw, L. P. et al. Niche and local geography shape the pangenome of wastewater- and livestock-associated Enterobacteriaceae. *Sci. Adv.* **7**, eabe3868 (2021).

21. Gao, Z. et al. Microneedle-mediated cell therapy. *Adv. Sci.* **11**, 2304124 (2023).

22. Chen, H. et al. Deep penetration of nanolevel drugs and micrometer-level T cells promoted by nanomotors for cancer immunochemotherapy. *J. Am. Chem. Soc.* **143**, 12025–12037 (2021).

23. Lu, X. et al. Single-atom catalysts-based catalytic ROS clearance for efficient psoriasis treatment and relapse prevention via restoring ESR1. *Nat. Commun.* **14**, 6767 (2023).

24. Wu, Y., Yuan, M., Song, J., Chen, X. & Yang, H. Hydrogen gas from inflammation treatment to cancer therapy. *ACS Nano* **13**, 8505–8511 (2019).

25. Steyn-Ross, M. L., Steyn-Ross, D. A. & Sleigh, J. W. Modelling general anaesthesia as a first-order phase transition in the cortex. *Prog. Biophys. Mol. Biol.* **85**, 369–385 (2004).

26. Awad, M. M. Comments on "Numerical simulation for MHD Williamson fluid utilizing modified Darcy's law". *Results Phys.* **16**, 102960 (2020).

27. Zhang, F. et al. Gastrointestinal tract drug delivery using algae motors embedded in a degradable capsule. *Sci. Robot.* **7**, eabo4160 (2022).

28. You, J. et al. Ultrarapid-acting microneedles for immediate delivery of biotherapeutics. *Adv. Mater.* **35**, 2304582 (2023).

29. Li, J., Esteban-Fernández de Ávila, B., Gao, W., Zhang, L. & Wang, J. Micro/nanorobots for biomedicine: Delivery, surgery, sensing, and detoxification. *Sci. Robot.* **2**, eaam6431 (2017).

30. Ye, Y., Yu, J., Wen, D., Kahkoska, A. R. & Gu, Z. Polymeric micro-needles for transdermal protein delivery. *Adv. Drug Deliv. Rev.* **127**, 106–118 (2018).

31. Fang, A. et al. Porous microneedle patch with sustained delivery of extracellular vesicles mitigates severe spinal cord injury. *Nat. Commun.* **14**, 4011 (2023).

32. Yasa, I. C., Ceylan, H., Bozuyuk, U., Wild, A.-M. & Sitti, M. Elucidating the interaction dynamics between microswimmer body and immune system for medical microrobots. *Sci. Robot.* **5**, eaaz3867 (2020).

33. Snieckute, G. et al. ROS-induced ribosome impairment underlies ZAKα-mediated metabolic decline in obesity and aging. *Science* **382**, eadf3208 (2023).

34. Zeng, J. et al. Nitric oxide controls shoot meristem activity via regulation of DNA methylation. *Nat. Commun.* **14**, 8001 (2023).

35. Joulia, E. & Metallo, C. M. Methionine and H_2S alter cancer–immune dialogue. *Nat. Metab.* **5**, 1456–1458 (2023).

36. Sridhar, V. et al. Light-driven carbon nitride microswimmers with propulsion in biological and ionic media and responsive on-demand drug delivery. *Sci. Robot.* **7**, eabm1421 (2023).

37. Zan, X. et al. Facile general injectable gelatin/metal/tea polyphenol double nanonetworks remodel wound microenvironment and accelerate healing. *Adv. Sci.* **11**, 2305405 (2024).

38. Yang, Z. et al. Thermal immuno-nanomedicine in cancer. *Nat. Rev. Clin. Oncol.* **20**, 116–134 (2023).

39. Yang, N. et al. Deep-learning terahertz single-cell metabolic viability study. *ACS Nano* **17**, 21383–21393 (2023).

40. Jin, L. et al. NIR-responsive MXene nanobelts for wound healing. *NPG Asia Mater.* **13**, 24 (2021).

41. Chen, Z. et al. Dual-responsive triple-synergistic Fe-MOF for tumor theranostics. *ACS Nano* **17**, 9003–9013 (2023).

42. Hu, T. et al. Layered double hydroxide-based nanomaterials for biomedical applications. *Chem. Soc. Rev.* **51**, 6126–6176 (2022).

43. Chu, D. et al. Dual-atom nanozyme eye drops attenuate inflammation and break the vicious cycle in dry eye disease. *Nano Micro Lett.* **16**, 120 (2024).

44. Ouyang, J. et al. In situ sprayed NIR-responsive, analgesic black phosphorus-based gel for diabetic ulcer treatment. *Proc. Natl. Acad. Sci. USA* **117**, 28667–28677 (2020).

45. Han, X. et al. Intelligent vascularized 3D/4D/5D/6D-printed tissue scaffolds. *Nano Micro Lett.* **15**, 239 (2023).

46. He, Z. et al. Resolvin D1 delivery to lesional macrophages using antioxidative black phosphorus nanosheets for atherosclerosis treatment. *Nat. Nanotechnol.* **19**, 1386–1398 (2024).

47. Zhu, Z. et al. Blue-ringed octopus-inspired microneedle patch for robust tissue surface adhesion and active injection drug delivery. *Sci. Adv.* **9**, eadh2213 (2023).

48. Beatty, R. et al. Soft robot–mediated autonomous adaptation to fibrotic capsule formation for improved drug delivery. *Sci. Robot.* **8**, eabq4821 (2023).

49. Veiseh, O. & Langer, R. A smart insulin patch. *Nature* **524**, 39–40 (2015).

50. Li, H. et al. Scattered seeding of CAR T cells in solid tumors augments anticancer efficacy. *Natl. Sci. Rev.* **9**, nwab172 (2022).

51. Yang, L. et al. Biofilm microenvironment triggered self-enhancing photodynamic immunomodulatory microneedle for diabetic wound therapy. *Nat. Commun.* **14**, 7658 (2023).

52. Li, X. et al. Transvascular transport of nanocarriers for tumor delivery. *Nat. Commun.* **15**, 8172 (2024).

53. Zhang, X. et al. AI-recognized mitochondrial phenotype enables Identification of drug targets. *Nat. Comput. Sci.* **4**, 563 (2024).

54. Yu, M. et al. Deep learning large-scale drug discovery and repurposing. *Nat. Comput. Sci.* **4**, 600 (2024).

Acknowledgements

Author contributions

Xingcai Zhang, Bin Zheng, Laiping Fang, and Qiuya Li contributed to the conceptualization and designed the experiments. Zhengyu Wu and Boxi Shen performed the microneedle preparation and cell biology experiments. Bowen Li performed image analyses. Xiaolu Cai, Yan Liu, and Yanhong Duo performed data analysis and validation. Bin Zheng and

Qiuya Li wrote the manuscript with input from all authors. Yang Bai, Shi-Xiang Cheng, and Xingcai Zhang supervised the overall study and revised the manuscript.

Competing interests

The authors declare no competing interest.

Additional information

Supplementary information The online version contains supplementary material available at
https://doi.org/10.1038/s41467-024-53280-8.

Correspondence and requests for materials should be addressed to Bin Zheng, Yang Bai, Shi-Xiang Cheng or Xingcai Zhang.

Peer review information *Nature Communications* thanks Wubin Bai, and the other anonymous reviewer(s) for their contribution to the peer review of this work. A peer review file is available.

Reprints and permissions information is available at
http://www.nature.com/reprints

Publisher's note Springer Nature remains neutral with regard to jurisdictional claims in published maps and institutional affiliations.